RSC Advances

PAPER

View Article Online
View Journal | View Issue

Cite this: *RSC Adv.*, 2025, **15**, 16035

Hydrothermal engineering of polyethylene glycol-assisted boron nitride/hematite nanohybrid composites for high-performance supercapacitors

Shamsiya Shams,†[a] B. Bindhu,*[a] Adhigan Murali, †[b] R. Ramesh, *[c] Abdullah Al Souwaileh[d] and Sung Soo Han*[b]

Developing high-performance energy storage materials is essential to meet the increasing global demand for sustainable energy solutions. In this study, a novel strategy is employed to synthesize polyethylene glycol-assisted boron nitride/hematite (PEG-BN/α-Fe_2O_3) hybrid composites through a hydrothermal process. Polyethylene glycol(PEG) serves as both a dispersant and a non-covalent linker that bridges hematite nanoparticles and BN sheets. With a combination of van der Waals interaction and hydrogen bonding with the component materials, PEG enables stable and homogeneous dispersion of hematite on the otherwise inert and agglomeration-prone BN surface. This dual interaction approach enables controlled interface engineering, solving one of the major challenges commonly faced in the synthesis of BN-based composites. It also acts as a functional modifier that modulates the interfacial interactions and regulates the nucleation and dispersion of α-Fe_2O_3 nanoparticles within the BN matrix. The incorporation of PEG enhanced the electrochemical and structural properties of the hybrid composite. Structural and morphological characterizations confirmed the uniform dispersion of α-Fe_2O_3 within the BN matrix, with PEG enhancing the interfacial interactions and overall material stability. TGA demonstrated that PEG incorporation significantly improved the thermal stability of the composites, delaying degradation and preserving structural integrity under high-temperature conditions. Electrochemical measurements, including CV and GCD analysis in a 6 M KOH electrolyte, revealed superior charge storage capabilities for PEG-BN/α-Fe_2O_3 compared to BN/α-Fe_2O_3. This hybrid composite exhibited a remarkable specific capacitance of 361.6 F g^{-1} at a current density of 3 A g^{-1}, significantly outperforming the individual components. The GCD studies display an enhanced charge retention capability of the hybrid composite with a coulombic efficiency of 83%, indicating reduced internal resistance and improved kinetics. Additionally, electrochemical impedance spectroscopy indicated a lower charge transfer resistance and enhanced conductivity in PEG-modified composites. The composite also retained 85% of its initial capacitance after 5000 cycles, demonstrating excellent cyclic stability. The improved electrochemical performance of PEG-BN/α-Fe_2O_3 hybrid composites is attributed to the synergistic effects of BN and α-Fe_2O_3, facilitated by PEG, which acts as a thermal buffer, prevents agglomeration, and enhances electrolyte–electrode interactions. These findings underscore the potential of PEG-assisted BN/α-Fe_2O_3 composites as advanced electrode materials for next-generation supercapacitors and other electrochemical storage devices.

Received 31st March 2025
Accepted 5th May 2025

DOI: 10.1039/d5ra02227d

rsc.li/rsc-advances

1 Introduction

Developing high-performance, affordable materials is crucial for advancing various fields from electronics to energy systems. To drive progress in science and technology, it is essential to discover new materials and composites and explore existing ones for novel applications. Energy storage systems are fundamental for the sustainable and efficient usage of energy resources.[1] These systems play a vital role in addressing the intermittency of renewable energy sources like wind and solar power, ensuring stability and enhancing the overall reliability of the energy infrastructure. Out of different energy systems,

[a]*Department of Physics, Noorul Islam Centre for Higher Education, Kumaracoil, Thuckalay, 629180, Tamilnadu, India. E-mail: bindhu.krishna80@gmail.com*
[b]*School of Chemical Engineering, Yeungnam University, 280 Daehak-Ro, Gyeongsan, 38541, Republic of Korea. E-mail: sshan@yu.ac.kr*
[c]*Department of Chemical Engineering, School of Mechanical, Chemical and Material Engineering, Adama Science and Technology University, Adama, P.O. Box-1888, Adama, Ethiopia. E-mail: ramesh.redrouthu@astu.edu.et*
[d]*Department of Chemistry, College of Science, King Saud University, Riyadh 11451, Saudi Arabia*
† Equally conributed.

electrochemical energy storage systems (eg, batteries and supercapacitors) are integral to modern energy applications, including electric vehicles, portable electronics, and grid stabilization.[2] The development of sustainable and advanced materials at a scalable level using straightforward facile synthesis methods, while ensuring their stability and efficiency, remains a significant challenge. Addressing this issue is critical for creating innovative materials that can meet the growing demands of modern applications without compromising environmental sustainability or economic feasibility. Two-dimensional (2D) materials offer a rich source of functional materials. Their unique structural and electronic properties make them up-and-coming candidates for next-generation devices.[3] Among these, hexagonal boron nitride(h-BN) and transition metal oxides (TMO) (eg, iron oxide, cobalt oxide, copper oxides, titanium oxides, *etc.*) stand out due to their abundance, low cost, and exceptional properties like thermal and chemical stabilities.[4]

In recent years, h-BN, a 2D material with alternating boron(B) and nitrogen atoms(N) in a honeycomb lattice arrangement, has been widely used in many energy systems as it indicates an improved efficiency of catalytic processes, particularly throughout the electrochemical reaction.[5] The layered structure of h-BN ensures the exfoliation into nanosheets, which is a versatile building block for next-generation devices. Chao Chen *et al.* demonstrated that the integration of h-BN to form a composite structure leads to enhanced specific capacitance and stabilities.[6] TMOs are recognized for their potential in energy storage due to their ability to undergo multiple oxidation states during electrochemical processes. Transition metal oxide composites, when hybridized with 2D materials such as boron nitride, exhibit improved capacitive performance but a suppressed faradaic signature due to enhanced conductivity and surface interactions.[7] Iron(III) oxide (α-Fe_2O_3/hematite) is a widely studied transition metal oxide and an active material in energy storage. Among the oxides of iron, Fe_3O_4(Magnetite) is more explored than α-Fe_2O_3. α-Fe_2O_3 is thermodynamically stable under typical surface conditions such as room temperature and atmospheric pressure.[8] The structural instability of α-Fe_2O_3 in the case of electrochemical operations, such as electrolyte interactions, potential fluctuations, *etc.*, ultimately leads to material degradation.[9] It is also evident that α-Fe_2O_3 exhibits certain limitations for energy application, including poor rate capability, limited surface area, cyclic stability, and structural stability.[10] To overcome these issues, α-Fe_2O_3 needs to be integrated with other 2D materials like h-BN and graphene, as these materials offer intriguing properties, thus enhancing superior performances. For instance, Yang *et al.* studied the preparation of electrodes of α-Fe_2O_3/rGO nanosheet composites with a specific capacitance of 320 F g^{-1} and a capacity retention of about 97% after 500 cycles.[11] Various synthesis routes, material modifications, and technologies are employed to design composite materials that could significantly impact the ionic and electronic transports in electrochemical systems.[12,13] Polyethylene glycol (PEG) has emerged as a versatile polymer in energy domains, as it is biocompatible and also ensures high solubility in various solvents. In energy systems, PEG frequently serves as a matrix for electrolytes, where it enhances ionic conductivity while preserving mechanical stability.[14] Integrating PEG into electrochemical devices like batteries and supercapacitors enables researchers to achieve notable performance, including cyclic stability and greater efficiencies.[15] Moreover, PEG-assisted composite materials support the development of stable interfaces, ensuring the durability and safety of energy systems.[16] Incorporating PEG-assisted modification in BN/α-Fe_2O_3 enhances the conductivity and electrochemical stability, thus mitigating the drawbacks faced by individual components.[17] Superior thermal conductivity is observed in PEG-assisted hybrid fillers compared to individual fillers, demonstrating the potential usage of PEG in enhancing the performance of hybrid fillers.[18] PEG grafted BN composites indicate significant improvement in the mechanical robustness and stability.[19] Dalal Hasan *et al.* investigated on PEG/α-Fe_2O_3 composites and ensured that incorporating PEG with α-Fe_2O_3 improves the optical and thermal properties of the composites.[20] Hybrid composites depict exceptional electrochemical activities.[21] The substantial surface area of BN enables the accommodation of a larger quantity of α-Fe_2O_3, thereby increasing the available active sites for electrochemical processes.[22] Doping techniques and surface functionalizations introduce more significant enhancements in the electrochemical performance of composites by efficiently improving the active sites, charge transfer mechanisms, and ion diffusion pathways.[23,24]

Developing new strategies to enhance the electrochemical performance of boron nitride remains a crucial challenge. In this context, integrating BN and α-Fe_2O_3 has emerged as a promising approach, offering synergistic effects for improved energy storage and conversion. However, the area remains unexplored, necessitating innovative material designs. To address this gap, we present the development of hybrid nanocomposites specifically, BN/α-Fe_2O_3 and PEG-assisted BN/α-Fe_2O_3 composites, engineered to optimize the electrochemical properties. Additionally, the incorporation of polyethylene glycol (PEG) further enhances the dispersion and material stability of the composites. This research work investigates the synthesis and electrochemical characterization of a novel composite material: PEG-assisted BN/α-Fe_2O_3 for supercapacitor application. The composite is prepared using the facile hydrothermal method and ultrasonication technique. The ultrasonication technique refines and homogenizes the components, enhancing their structural and electrochemical properties. PEG-BN/α-Fe_2O_3 mixture underwent hydrothermal treatment to facilitate the formation of a composite material with superior properties. The hydrothermal method is employed as it provides a controlled environment, high-pressure, and high-temperature systems under sealed conditions, thus enabling the growth of well-defined nanocomposites with precise morphologies. This synthesis approach is advantageous in synthesizing composites, as it ensures good dispersion and interaction between the components. A comprehensive analysis, including structural, morphological, and electrochemical studies, is conducted on the prepared samples, and the obtained results are thoroughly discussed to

understand their characteristics and performance. This work represents a significant contribution to advancing functional nanomaterials for electrochemical energy storage and conversion.

2. Experimental section

2.1 Materials

Hexagonal boron nitride powder (AR grade, 99%), iron(III) oxide nanopowder (AR grade, 99%), and polyethylene glycol (PEG) with a molecular weight of 4000g mol^{-1} were procured from Sigma Aldrich, USA. Deionized water and dimethyl formamide (DMF) were sourced from Merck.

2.2. Synthesis of BN, PEG-BN/α-Fe_2O_3, and BN/α-Fe_2O_3 composites

The liquid-phase exfoliation process is introduced to exfoliate h-BN.[25] Bulk h-BN is dispersed in DMF and undergoes stirring for about 45 minutes, followed by an ultrasonication process to disrupt the interlayer forces between the h-BN structure, promoting the formation of individual BN layers. This mixture is then subjected to a centrifugation process(3500 rpm) to eliminate unexfoliated bulk h-BN material. The exfoliated BN was oven-dried at a temperature of 70 °C for 48 hours to remove the residual solvent. Separately, a PEG solution of a 1 : 3 volume ratio is prepared with deionized water. To this PEG solution, α-Fe_2O_3 nanoparticles are added, and the mixture undergoes vigorous stirring for about 1 hour to ensure the homogeneity of the suspended particles. Following this, previously prepared BN is added to the PEG-α-Fe_2O_3 solution and stirred for an additional 1 hour to facilitate the mixing between the components. This well-mixed suspension is then subjected to microwave-assisted ultrasonication for 2 hours. This method initiates rapid and efficient heating, further enhancing the dispersion and thus minimizing agglomerations. The final synthesis step involves the hydrothermal treatment of the solution. The mixture is then transferred to a Teflon-lined autoclave and subjected to hydrothermal conditions (120 °C, 5 hours). The elevated temperature, pressure, and time duration within the autoclave aid in the formation of well-defined nanocomposites and also improve the interaction between the subsequent components. The autoclave is then allowed to cool at room temperature. After hydrothermal treatment, the mixture is subjected to centrifugation (4000 rpm), washed with distilled water and ethanol, and oven-dried at 100 °C for 7 hours. The resultant product (PEG-BN/α-Fe_2O_3) is carefully removed, ground into fine powders, and sealed in zip-lock covers for further analysis. A control sample (BN/α-Fe_2O_3) is also prepared by following the same procedure, excluding the addition of PEG to the synthesis process. This control sample also provides a comparative analysis of the composites, enabling a better understanding of the composite and its performance.

2.3 Material characterization

The thermal stability of the samples is evaluated using SIINT 6300 T, a German thermogravimetric (TGA) analysis system. The measurements were carried out under a nitrogen atmosphere. Approximately 5 mg of the sample is used for each experiment. To determine the crystalline structure and particle size of the composites, X-ray diffraction (XRD) is performed using X'Pert Pro-PANalytical. The analysis is conducted with CuKα radiation (λ = 1.5406 A) over a 2θ range of 10–80°. The structural and morphological characteristics of the synthesized nanoparticles were examined using Field emission scanning electron microscopy (FESEM) by SIGMA HV-Carl Zeiss with Brucker Quantax 200-Z0EDS detector instrument. Raman spectroscopy is further employed to analyze the structural properties of the material. The Raman spectra were recorded using an XPLORA PLUS, Horiba, France, Raman spectrometer. Additionally, the chemical bonds and functional groups present in the sample are determined by Fourier transform Infrared spectroscopy (FTIR) with a Bruker Alpha T, Germany FTIR instrument. The electrical properties are analyzed through current–voltage (*I–V*) measurements and are conducted using a Keithley 2401 system. UV-visible (UV-vis) analysis technique is implemented to determine the electronic structure, bandgap energy, *etc.* of the synthesized composites with the help of Systronics, 2202, India UV-visible spectrophotometer instrument. These comprehensive characterization techniques ensured a detailed understanding of the material's structural, morphological, and functional properties, essential for optimizing its performance in various applications.

2.4. Electrochemical characterization

The electrochemical characteristics of the samples are analyzed using cyclic voltammetry (CV) analysis, galvanostatic charge–discharge (GCD) testing, and Electrochemical impedance spectroscopy (EIS). These experiments were conducted in a conventional three-electrode system, controlled by an Origalys OGF01A electrochemical workstation. In this setup, an Ag/AgCl electrode functions as a reference electrode, and a platinum wire is used as a counter electrode. The following methods were utilized to synthesize the working electrode. Initially, a homogenous slurry is formulated by thoroughly mixing 80wt% of the electroactive material (PEG-BN-α-Fe_2O_3 and BN-α-Fe_2O_3), 15wt% of conductive carbon and 5wt% polyvinylidene fluoride (PVDF) in a 10% solution of *N*-methyl-2 pyrrolidone (NMP) solvent this composition ensures optimal electron transport, mechanical stability and effective binding of the active material. 1 mg of this prepared slurry is then uniformly deposited onto a graphite sheet, serving as the current collector, *via* the drop-casting technique. The mass of active material deposited per electrode is approximately 0.80 mg. The coated electrodes were subsequently subjected to vacuum drying at 80 °C overnight to eliminate the residual solvent and enhance the adhesion between the active material and the substrate. This method also improves the uniformity and stability of the electrode surface for electrochemical characterization. All analyses were carried out at room temperature. Aqueous electrolytes are often preferred due to their availability, low toxicity, cost-effectiveness, and ease of handling. To investigate the electrochemical behavior of the synthesized samples, including their

capacitive behavior and efficiencies, a 6 M potassium hydroxide (KOH) aqueous electrolyte is utilized. The CV scans are recorded at different scan rates of 10 mV s^{-1}, 25 mV s^{-1}, 50 mV s^{-1}, and 100 mV s^{-1} consecutively. The GCD studies are also carried out at different current densities varying from 3 A g^{-1} to 6 A g^{-1}, respectively. A potential window of 0.1 to 0.5 V is maintained for all electrochemical measurements.

3. Results and discussion

3.1 Mechanistic insights into the formation of PEG-BN/α-Fe_2O_3 composites

The stepwise formation of PEG-BN/α-Fe_2O_3 and BN/α-Fe_2O_3 hybrid composites is illustrated in Scheme 1. The exfoliation process of BN increases the surface area and exposes active sites for the attachment of α-Fe_2O_3 nanoparticles. The aqueous PEG solution stabilizes the BN/α-Fe_2O_3 composites, preventing their agglomeration through steric hindrance. The PEG molecules adsorb onto the boron nitride(BN) surface. The α-Fe_2O_3 particles are combined with the PEG chains *via* coordination of Fe^{3+} ions. Resulting in the formation of the final hybrid composite structure. The process can be represented as:

$$BN_{surface} - OH + HO - (CH_2CH_2O)_n - H \xrightarrow{\text{Hydrogen bonding}} BN\ldots PEG \quad (1)$$

The α-Fe_2O_3 nanoparticles possess Fe^{3+} ions on their surface that coordinate with the lone pair of the ether oxygen groups present in PEG.

$$Fe_{surface}{}^{3+} + -OCH_2CH_2 \rightarrow Fe^{3+}\ldots O\text{-}PEG \quad (2)$$

This indicates a strong anchor of α-Fe_2O_3 nanostructures with PEG. The well-dispersed PEG-BN/α-Fe_2O_3 suspension undergoes hydrothermal treatment at 120 °C in an autoclave, resulting in the nucleation and controlled growth of α-Fe_2O_3 nanoparticles on the BN surface. The BN nanosheets provide nucleation sites, as they possess a high surface area and chemical stability, further improving the adhesion and subsequent growth of α-Fe_2O_3 nanoparticles.[26] At 120 °C (hydrothermal treatment), α-Fe_2O_3 epitaxially bonds on the BN surface, resulting in controlled nucleation.[27] PEG is used as a stabilizing and structure-directing agent that helps in the uniform dispersion of α-Fe_2O_3, thus favoring nucleation and controlled growth.[28] The electrostatic interactions facilitate the attachment of Fe^{3+} on the negatively charged BN surface.[29,30] The zeta potential measurements of boron nitride range between −26 mV to −52 mV, respectively, providing experimental evidence on the negativity of boron nitride[31–33]. The hydrolysis reaction in the aqueous solution leads to minimal $Fe(OH)_3$ precipitation, which further undergoes dehydration to form α-Fe_2O_3 nanoparticles upon heating. It is also evident that PEG formed hydrogen bonds with both BN and α-Fe_2O_3, enhancing adhesion and further contributing to the stability of the composite.

The overall reaction pathway for the composite synthesis is summarized as:

$$PEG + BN + \alpha\text{-}Fe_2O_3 + H_2O \xrightarrow[120^\circ C]{\text{Hydrothermal}} \text{PEG-BN/}\alpha\text{-}Fe_2O_3 \text{ composite} \quad (3)$$

3.2 Morphology and structure of the composites

The X-ray diffraction analysis (XRD) is a powerful technique for characterizing the crystalline structure, phase composition, and degree of crystallinity in materials. Fig. 1 represents the XRD pattern of BN/α-Fe_2O_3 composites and composites, respectively. The XRD peaks of α-Fe_2O_3 nanoparticles exhibit characteristic peaks at 24.20°, 33.23°,35.70°, 49.57°,54.20° and 64.15° following the (012), (104), (110), (024), (116), (300) crystal planes, respectively. These peaks align well with the crystal structure of

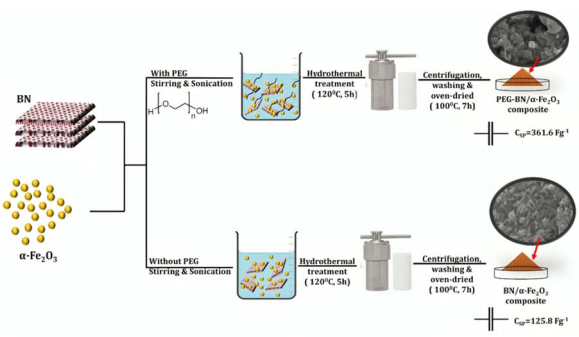

Scheme 1 Experimental setup for the hydrothermal synthesis of PEG-BN/α-Fe_2O_3 and BN/α-Fe_2O_3 hybrid composites.

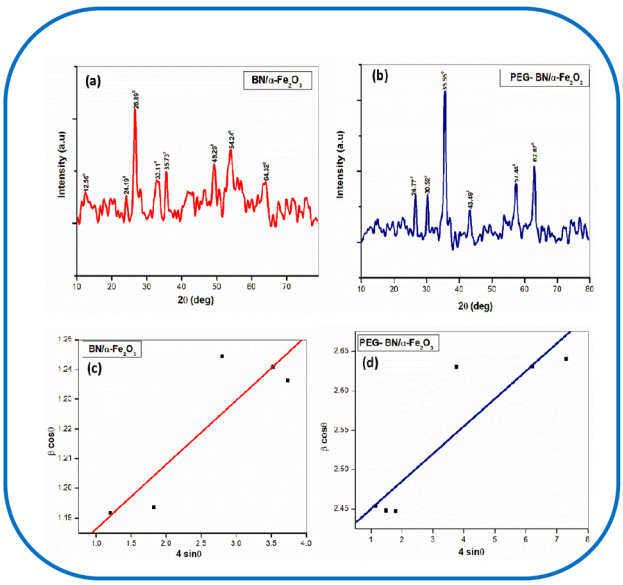

Fig. 1 XRD analysis of hydrothermal method-assisted synthesis of (a) BN/α-Fe_2O_3 composites, (b) PEG-BN/α-Fe_2O_3 composites. Williamson–Hall analysis plotted between 4 sin θ against β cos θ of (c) BN/α-Fe_2O_3 and (d) PEG-BN/α-Fe_2O_3 produced using the hydrothermal synthesis route.

α-Fe_2O_3, as referenced in the JCPDS card no 01-089-05961.[15] The XRD pattern exhibits a high-intensity peak at 26.61°, consistent with the (002) *hkl* plane of boron nitride as indexed in the JCPDS database (Reference no: 34-0421).[34] This confirms the presence of exfoliated boron nitride within the composite material.

Fig. 1(a) illustrates the XRD analysis of BN/α-Fe_2O_3. The characteristic peaks are obtained at 12.500, 24.190, 26.890, 33.110, 35.730, 49.610, 54.010, and 64.320 respectively. The peaks represent the characteristic diffractions corresponding to both α-Fe_2O_3 and exfoliated boron nitride phases. The XRD pattern of PEG-BN/α-Fe_2O_3 composites depicts the peaks at 26.350, 30.520, 35.550, 43.490, 57.300, and 62.870 (Fig. 1(b)). The distinct peaks depict the crystalline structure, indicating the successful incorporation of exfoliated BN with α-Fe_2O_3 without disrupting the fundamental phase structure of either component. Minor changes in the peak intensity and slight shifts in the peaks are observed in PEG-BN/α-Fe_2O_3 composites due to the influence of PEG in the synthesis of the composite. The PEG molecules absorb onto the BN surface, causing a disruption, thus weakening the intensity of the BN characteristic peak as compared to that of BN/α-Fe_2O_3 composites.

The average crystallite size of the synthesized material is calculated using the Debye–Scherrer formula,

$$D = k\lambda/\beta \cos\theta \quad (4)$$

The XRD patterns of both samples exhibit broad diffraction peaks. The assessment of the crystallite size, derived from the peak broadening in the XRD patterns, suggests that the crystal domains fall within the nanoscale range. A significant reduction in the crystallite size is observed for PEG-BN/α-Fe_2O_3 composites, 9.3 nm compared to the composite without PEG, 14.45 nm. This indicates that PEG plays a crucial role as a surfactant and dispersing agent by hindering the agglomeration of BN and α-Fe_2O_3 nanoparticles. To quantitatively distinguish the contributions of crystallite size and strain to the observed peak broadening and intensity variations, the Williamson–Hall(W–H) plot approach is employed. This method utilizes the following equation given below:

$$\beta \cos\theta = k\lambda/D + 4\varepsilon \sin\theta \quad (5)$$

where 'β' is the full width at half maximum, FWHM value, 'θ' is the Bragg angle, and 'ε' is the microstrain, respectively. A linear relationship graph is obtained when $\beta \cos\theta$ is plotted against $4\varepsilon \sin\theta$. The crystallite size (D) is determined from the y-intercept ($k\lambda/t$), and the microstrain is obtained from the slope of the line. Fig. 1(c and d) shows the W–H plot of BN/α-Fe_2O_3 and PEG-BN/α-Fe_2O_3 composites. The analysis mentions that the W–H plot of the samples demonstrates positive slopes. The positive slope indicates a small amount of tensile strain in the composites.[35] It also increases the interplanar distances, potentially increasing the conductivity of the prepared composites. Fig. 1(c), exhibits the W–H plot of BN/α-Fe_2O_3. The W–H plot of PEG-BN/α-Fe_2O_3 is shown in Fig. 1(d) and it reveals a lower lattice strain, as PEG aids in the reduction of internal strains within the composite material.

The dislocation density(ρ), a measure of the defects (specifically dislocations), in the crystal lattice, is calculated using the formula,

$$\rho = 1/D^2 \quad (6)$$

where 'D' displays the corresponding crystallite size of the sample. The defect concentration in the sample is reflected by the magnitude of the dislocation density values, which are presented in Table 1. A lower dislocation density signifies an enhanced crystalline quality.[36] The mechanical and electronic properties of the as-synthesized composites are significantly affected by the internal strain that develops within the material. The presence of α-Fe_2O_3 nanoparticles reinforces the BN matrix, improving the overall integrity and mechanical stability of the composites.

The FTIR analysis is performed to investigate the functional groups, molecular interactions, and structural modifications of α-Fe_2O_3, BN/α-Fe_2O_3, and PEG-BN/α-Fe_2O_3 composites as depicted in Fig. 2(a). The Fe–O stretching vibrations in α-Fe_2O_3 are observed at 432.9 cm^{-1} and 533.6 cm^{-1}.[37,38] The absence of significant peaks in the higher wavenumber region indicates that the sample consists primarily of α-Fe_2O_3 without any organic functional groups. A strong adsorption band at 1388.8 cm^{-1} and 1401.9 cm^{-1} in BN/α-Fe_2O_3 and PEG-BN/α-Fe_2O_3 composites corresponds to the B–N stretching vibrations, confirming the incorporation of boron nitride into the composite. A broad adsorption band at 3454.8 cm^{-1} depicts the hydrogen bonding interactions between PEG and BN/α-Fe_2O_3 components in the composite, corresponding to hydroxyl groups (O–H stretching vibrations) in PEG. The shift in peak positions and broadening effects exhibit strong molecular interactions that enhance the composite's stability. The higher peak intensity in PEG-BN/α-Fe_2O_3 is due to the presence of PEG polymer, as it has numerous C–H, C–O, and O–H bonds that contribute well to the FTIR spectrum consecutively.[39]

The Raman spectra elucidate the molecular interactions, vibrational modes, and phase composition of BN/α-Fe_2O_3 and PEG-BN/α-Fe_2O_3 composites and are shown in Fig. 2(c and d). The most intense peaks in α-Fe_2O_3 appear between 1320 cm^{-1} and 1350 cm^{-1} respectively. In Fig. 2(c), BN and α-Fe_2O_3 interact through surface bonding (Fe–O–B) interactions at the interface. The lower frequency peak at 387.1 cm^{-1} is attributed to the E_g symmetric vibrations of the Fe–O bonds in hematite. Compared to pure hematite, the Fe–O stretching vibrations in the composite are slightly shifted. The in-plane B–N stretching vibrations in BN correspond to the 1365 cm^{-1} adsorption peaks. A newer peak at 1609.4 cm^{-1} corresponds to the C–H bending

Table 1 Structural parameters of PEG-BN/α-Fe_2O_3 and BN/α-Fe_2O_3 composites prepared using the hydrothermal synthesis method

Sample	Average crystallite size, D (nm)	Strain, ε (%)	Dislocation density, $\rho \times 10^{14}$ lines per m^2
PEG-BN/α-Fe_2O_3	9.3	1.716	0.0115
BN/α-Fe_2O_3	14.45	2.415	0.0048

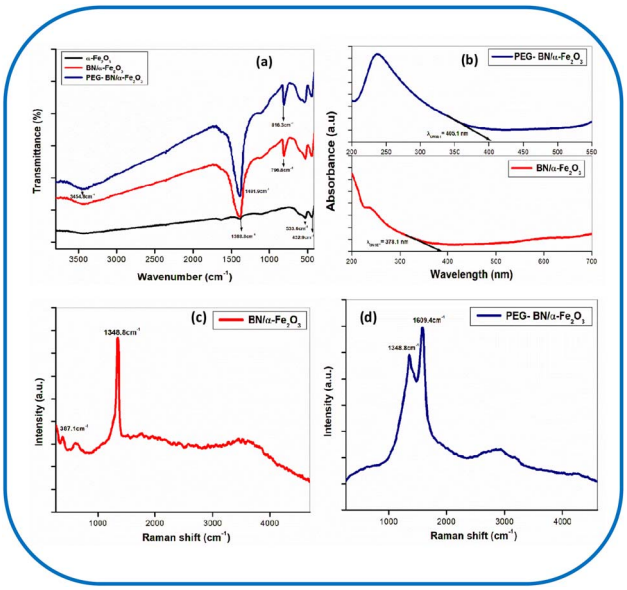

Fig. 2 FTIR spectra of (a) α-Fe_2O_3, BN/α-Fe_2O_3, and PEG-BN/α-Fe_2O_3, UV-visible absorption spectra of (b) BN/α-Fe_2O_3 and PEG-BN/α-Fe_2O_3, Raman spectra of (c) BN/α-Fe_2O_3 and (d) PEG-BN/α-Fe_2O_3.

vibrations from PEG, confirming its incorporation into BN/α-Fe_2O_3(Fig. 2(d)). The comparison of Raman spectral shifts between the samples and their interpretation is discussed in Table 2. It is also noted that the peak shifts to the higher Raman shift region suggest the presence of tensile strain, consistent with the findings from the Williamson–Hall plot analysis.

The UV-visible spectrum(absorbance v/s wavelength) measures the absorption and transmission of light and provides information about the electronic transitions, optical band gap, and molecular interactions within the materials. The UV-visible spectral analysis of BN/α-Fe_2O_3 and PEG-BN/α-Fe_2O_3 composites is shown in Fig. 2b. The energy band gap of α-Fe_2O_3 is reported between 2 eV to 2.5 eV respectively.[40] The band gap of BN is about 6.02 eV, indicating an insulating nature.[41] When hematite is integrated with exfoliated BN, significant modifications occur in the electronic structure of the composite material. When BN and α-Fe_2O_3 are combined, their energy levels align in such a way as to facilitate the charge transfer between the two materials. The composite of these two materials initiates an electronic coupling at the interface, allowing partial charge delocalization, which overall lowers the bandgap energy of their composite materials.

The λ_{onset} values of BN/α-Fe_2O_3 and PEG-BN/α-Fe_2O_3 composites are determined from the spectral analysis, and the corresponding bandgap energies are calculated using the equation,

$$E_g = hc/\lambda_{onset} \quad (7)$$

where 'h' is Planck's constant, 'c' is the speed of light, and 'λ_{onset}' is the absorption onset wavelength. The λ_{onset} value of BN/α-Fe_2O_3 composites is 378.1 nm, and the corresponding bandgap energy is 3.28 eV successively. PEG-BN/α-Fe_2O_3 composites depict a λ_{onset} value of 405.1 nm and a bandgap energy of 3.06 eV. The presence of PEG leads to a decrease in the bandgap in PEG-BN/α-Fe_2O_3 when compared to BN/α-Fe_2O_3, as it helps to alter the charge carrier dynamics, facilitating better electronic interaction and recombination rates within the composite materials. PEG influences the interaction between BN and α-Fe_2O_3 by acting as a surfactant and stabilizer, improving dispersion and reducing surface defects.[42] The polymer chains further modify the local dielectric environment, leading to a redistribution of the electronic states at the BN/α-Fe_2O_3 interface, introducing improved electron mobility, altering the band structure, and lowering the energy band gap.[45] The Tauc plot is a widely used method to determine the optical bandgap of materials by analyzing their adsorption coefficient(α) as a function of photon energy($h\nu$). The Tauc plot of BN/α-Fe_2O_3 and PEG-BN/α-Fe_2O_3 composites is illustrated in Fig. 3. The equation governing this method is

$$(\alpha h\nu)^2 = A\,(h\nu - E_g) \quad (8)$$

where 'E_g' is the bandgap energy, and 'A' is the proportionality constant. By extrapolating the linear portion of the plot to the x-axis the optical bandgap E_g is determined. The E_g values of BN/α-Fe_2O_3 and PEG-BN/α-Fe_2O_3 composites are found to be at 3.51 eV and 3.01 eV from the Tauc plot analysis, which is in agreement with the band gap energies calculated from UV-visible spectroscopic data as demonstrated in Table 3.

The TGA analysis of BN, α-Fe_2O_3, BN/α-Fe_2O_3, and PEG-BN/α-Fe_2O_3 composites is depicted in Fig. 4. The TGA curve of BN demonstrates a minimum weight loss, signifying its excellent thermal stability. The onset degradation temperature (ODT) of BN is at 201.93 °C, indicating its superior resistance to thermal

Table 2 The Raman spectral shifts and interpretation of PEG-BN/α-Fe_2O_3 and BN/α-Fe_2O_3 composites synthesized using the hydrothermal method

Peaks (cm^{-1})	PEG-BN/α-Fe_2O_3 composites	BN/α-Fe_2O_3 composites	Interpretation
387.1	Present	Present	The Fe–O stretching mode is retained in all composites
1348.8	Present (slight shift)	Present (slight shift)	BN E_{2g} mode was retained, but slight shift due to Fe–O–B and PEG interactions
1609.4	Present	Absent	C–H bending from PEG, confirming its integration in the composite

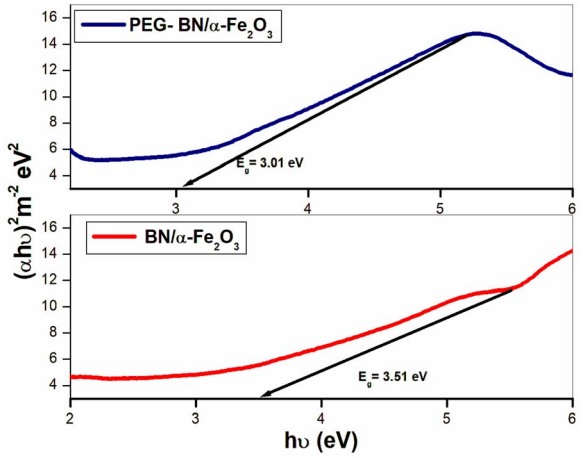

Fig. 3 Tauc plot analysis of BN/α-Fe_2O_3 and PEG-BN/α-Fe_2O_3 composites synthesized *via* the hydrothermal method, illustrating their optical bandgap.

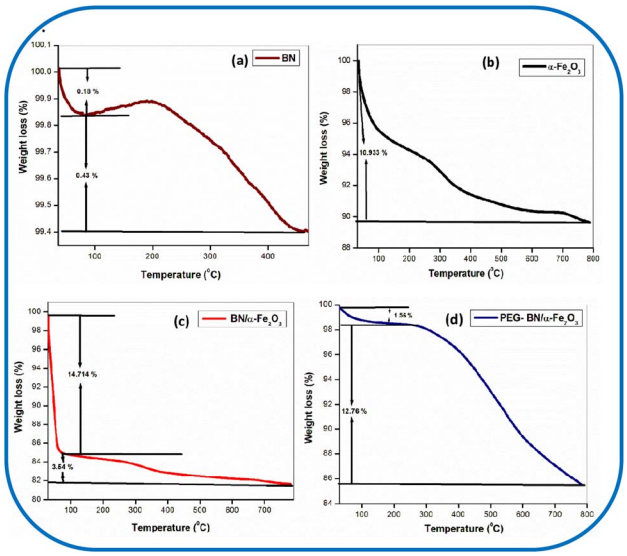

Fig. 4 TGA plot (Temperature v/s Weight loss), of (a) BN, (b)α-Fe_2O_3, (c)BN/α-Fe_2O_3, and (d)PEG-BN/α-Fe_2O_3 composites prepared using the hydrothermal technique.

decomposition (Fig. 4(a)). Fig. 4(b) exhibits that α-Fe_2O_3 specifies a progressive weight loss of 10.93% over the temperature range studied, primarily due to the removal of surface-bound water and other residuals. The ODT of α-Fe_2O_3 is observed at 100.87 °C and the ODT for BN/α-Fe_2O_3 is 114.2 °C, showing improved stability compared to that of α-Fe_2O_3 but reduced stability relative to BN(Fig. 7(c)). PEG-BN/α-Fe_2O_3 demonstrates an ODT OF 304.98 °C as shown in Fig. 4(d). The degradation involves the breaking of C–C bonds and C–O bonds in the polymer chain, leading to the formation of volatile products and resulting in significant weight loss in the TGA curve. It is also noted that PEG-BN/α-Fe_2O_3 composites show enhanced thermal stability out of all the composites, including BN, as PEG acts as a thermal buffer, delaying the degradation and preventing the rapid decomposition of BN and α-Fe_2O_3, thus enhancing the interfacial bonding, which stabilizes the composite structure under high-temperature conditions.

The morphology and size of the particles are analyzed using FESEM analysis as displayed in Fig. 5. The FESEM images of BN/α-Fe_2O_3 illustrate the surface morphology at different magnifications in Fig. 5(a–c) respectively. The particles predominantly display a rod-like elongated morphology, characteristic of α-Fe_2O_3 while BN provides a supporting matrix, potentially enhancing the structural integrity and stability. The estimated particle size with an average diameter falls between 20–40 nm for PEG-BN/α-Fe_2O_3 and BN/α-Fe_2O_3 composites. The uniform dispersion of hematite within BN exhibits a strong interfacial interaction likely due to hydrogen bonding and electrostatic forces developed during hydrothermal synthesis. The FESEM micrographs of PEG-BN/α-Fe_2O_3 showcase the surface morphology progressively at higher magnifications (Fig. 5(d–f)) consecutively. The FESEM analysis demonstrates that PEG-BN/α-Fe_2O_3 significantly improves the morphology and dispersion of BN/α-Fe_2O_3 composites. Well-dispersed spherical-shaped nanoparticles are observed in PEG-BN/α-Fe_2O_3 composites. The polymer chains of PEG produce a steric hindrance effect, which resists the random elongation of crystals, leading to spherical structures.[46]

3.3 Electrochemical analysis

The cyclic voltammetry (CV) is conducted to analyze the electrochemical behavior of PEG-BN/α-Fe_2O_3 and BN/α-Fe_2O_3 composites. The experiments were performed in 6 M KOH electrolyte, within a set voltage ranging from 0 to 0.5 V. Cyclic voltammetry curves of PEG-BN/α-Fe_2O_3 and BN/α-Fe_2O_3 composites at different scan rates are depicted in Fig. 6. The CV curves display a quasi-rectangular shape reflecting a capacitive charge storage process that derives considerable contributions from electric double-layer capacitance and pseudocapacitance. Even though the CV curves lack well-defined, sharp redox peaks,

Table 3 UV-visible and Tauc plot analysis PEG-BN/α-Fe_2O_3 and BN/α-Fe_2O_3 composites synthesized using the hydrothermal route

Samples	Absorption onset wavelength, λ_{onset} (nm)	Bandgap Energy (eV) from λ_{onset} calculations (eV)	Tauc plot, bandgap energy (eV)
BN	210–215	—	5.9 (ref. 43)
α-Fe_2O_3	496–590	—	2.1–2.5 (ref. 44)
PEG-BN/α-Fe_2O_3	405.1	3.06	3.01
BN/α-Fe_2O_3	378.1	3.28	3.51

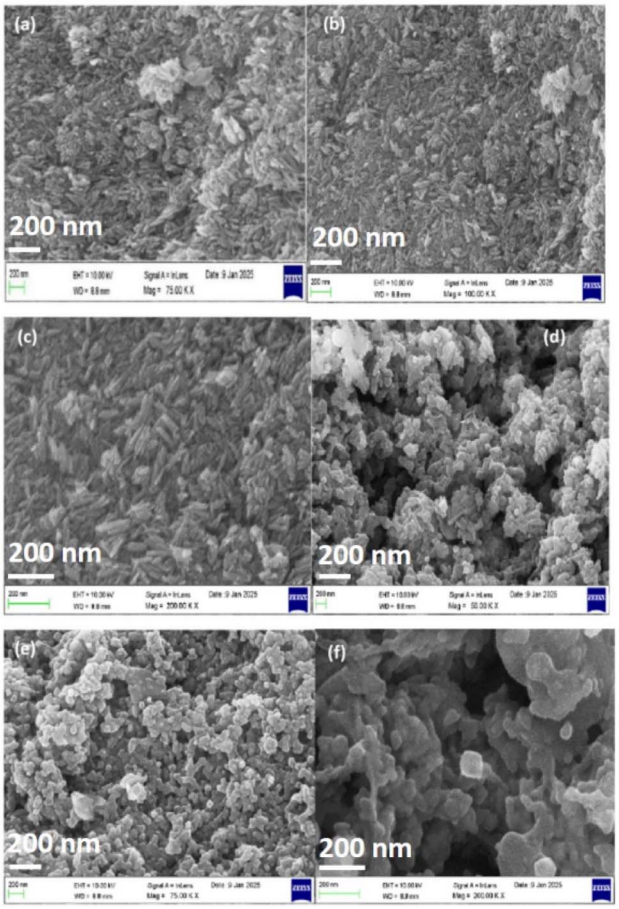

Fig. 5 SEM micrographs of (a), (b) and (c) BN/α-Fe_2O_3 and (d). (e) and (f) PEG-BN/α-Fe_2O_3 at different magnifications produced using the hydrothermal process.

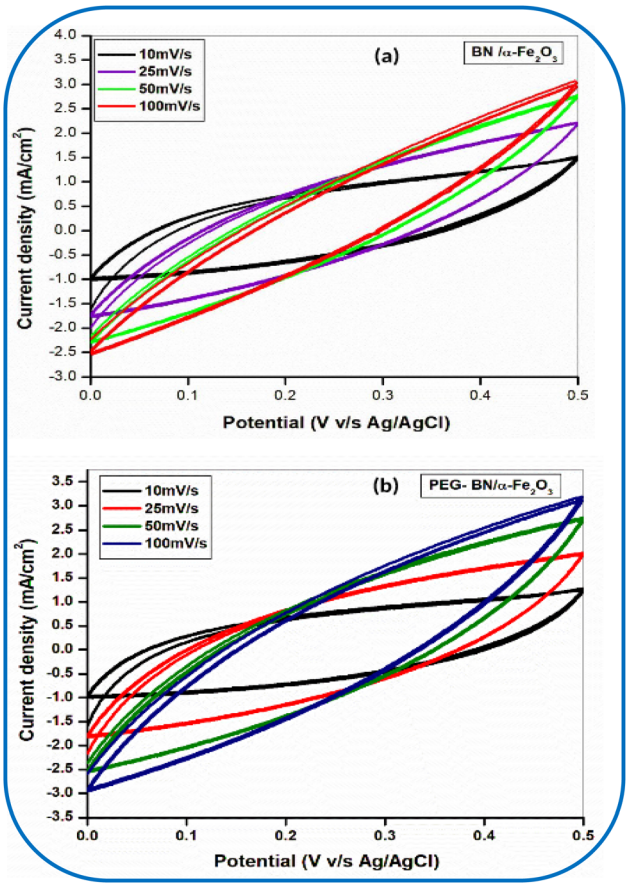

Fig. 6 Cyclic voltammetry analysis of (a) BN/α-Fe_2O_3, (b) PEG-BN/α-Fe_2O_3 composites produced by the hydrothermal procedure.

vague broad redox features related to faradaic reactions of α-Fe_2O_3 exist below the rectangular profile, which is an indicator of surface-confined redox activity, a capacitive charge storage process. Fig. 6(a) shows the CV curve of BN/α-Fe_2O_3 composites. BN provides surface area for the accumulation of more charge, enhancing the capacitance of the composite. The PEG-BN/α-Fe_2O_3 exhibits superior electrochemical performance to BN/α-Fe_2O_3 composites, as displayed in Fig. 6(b).

The larger CV area of PEG-BN/α-Fe_2O_3 indicates higher capacitance and charge storage capabilities. PEG also improves the electrode–electrolyte interaction, leading to better stability and cyclic performance than BN/α-Fe_2O_3 composites. PEG contains an ether functional group that configures hydrogen bonds with polar electrolytes and water molecules, thus enhancing the wettability and dispersibility of the electrode material in the electrolyte, enabling effective penetration of the electrolyte in the electrode structure.[47] This improves the ion transport and reduces interfacial resistance, ultimately resulting in enhanced electrochemical performance.[48] The redox mechanisms in this composite involve the faradaic charge storage mechanism, facilitated by α-Fe_2O_3, and are further enhanced by the synergistic effects of BN and PEG, respectively.

In an alkaline electrolyte (KOH), α-Fe_2O_3 undergoes two-step redox reactions:

During the charging process,

$$\alpha\text{-}Fe_2O_3 + OH^- + H_2O + e^- \rightarrow Fe(OOH) + 2OH^- \quad (9)$$

This reaction shows that α-Fe_2O_3 reacts with hydroxide ions (OH^-) from the KOH electrolyte and water molecules to form FeOOH (iron oxyhydroxide) and release hydroxide ions.

During the discharging process,

$$FeO(OH) + e^- \rightarrow FeOOH \quad (10)$$

$$2FeOOH + 2e^- \rightarrow \alpha\text{-}Fe_2O_3 + H_2O \quad (11)$$

Unlike iron oxides like Fe_3O_4, α-Fe_2O_3 is preferred due to its relative stability and well-defined electrochemical behaviors in alkaline electrolytes.[49] BN also contributes to the structural stability of the composite materials, improving the electron mobility, chemical stability, and electrical conductivity, and preventing particle agglomeration, enhancing the electrolyte accessibility to α-Fe_2O_3.[50] The minimal variation in CV curve shape with increasing sweep rate indicates the outstanding charge storage capability and improved capacitive performance of the synthesized materials.[51]

The galvanostatic charge–discharge analysis is shown in Fig. 7 for BN, α-Fe_2O_3, BN/α-Fe_2O_3, and PEG-BN/α-Fe_2O_3 composites, conducted at different current densities, 1 A g^{-1}, 3 A g^{-1}, 5 A g^{-1}, and 5.5 A g^{-1}, respectively, within a potential window between 0 to 0.5 V. The chosen current densities between 1 A g^{-1} to 5.5 A g^{-1} are common standard values in electrochemical investigations of composite electrode materials, especially for transition metal oxides and boron nitride systems, to assess rate capability and cycling stability.[52] Fig. 7(a) depicts the GCD curve for BN and α-Fe_2O_3. The GCD curves of both BN and α-Fe_2O_3 indicate a non-faradaic capacitive behavior with low electrochemical interactions. A main indicator used to evaluate the effectiveness of a material in electrochemical applications is its capacity to store and release charge, denoted as the specific capacitance (C_{SP}). The C_{SP} value is directly related to the charge–discharge duration observed in the GCD curves. Quantitatively, specific capacitance is determined by the formula;

$$C_{SP} = i \times \Delta t/m \times \Delta V \quad (12)$$

where 'C_{SP}' is the specific capacitance value (F g^{-1}), 'm' is the mass of the active material(gm), 'i' represents the discharge current (in amperes(A)), 'ΔV' corresponds to the potential difference (in Volts(V), 'Δt' denotes the discharge time (in seconds(s)) correspondingly. A larger C_{SP} value directly reflects an enhanced capacity for charge storage and delivery per unit mass of the electrode. A nearly triangular shape in the GCD curve signifies an electric double-layer capacitance (EDLC) nature.[53] In contrast, a deviation from the triangular shape and a plateau-like region indicates a pseudocapacitive behavior.[54] BN contributes an EDLC behavior (electrostatic interactions), and α-Fe_2O_3 provides pseudocapacitive behaviors and faradaic charge transfer *via* redox reactions, representing a hybrid supercapacitor. The C_{SP} of BN and α-Fe_2O_3 at a current density of 1 A g^{-1} is at 12.18 F g^{-1} and 17.64 F g^{-1} respectively. Fig. 7(b) and (c), present the GCD curve of BN/α-Fe_2O_3 composites at varying current densities. The composite exhibits specific capacitance values of 125.8 F g^{-1} at 3 A g^{-1} and 90.44 F g^{-1} at 5 A g^{-1} indicating a notable improvement over the individual components. Additionally, Fig. 7(d and e) illustrates the GCD curves of PEG-BN/α-Fe_2O_3, which demonstrate significantly enhanced capacitance, achieving 361.6 F g^{-1} at 3 A g^{-1} and 303.50 F g^{-1} at 5.5 A g^{-1}. These C_{SP} values highlight the superior electrochemical performance of the PEG-BN/α-Fe_2O_3 composites. The GCD measurements also revealed that the PEG-BN/α-Fe_2O_3 composite exhibits an energy density of 18.08 Wh per kg, indicating its suitability for supercapacitor applications. The interconnected network of BN and α-Fe_2O_3 also reduces charge transfer resistance, ensuring more efficient electron movement and improved electrochemical performance. The composite structure of PEG-BN/α-Fe_2O_3 enhances mechanical stability, preventing electrode degradation during repeated charge–discharge cycles. The graphical representation of the composites is depicted in Fig. 7(f). A comparison study of the electrochemical performances of BN and α-Fe_2O_3 material-based composites is shown in the Table 4.

The higher coulombic efficiency of PEG-BN/α-Fe2O3 (83%) shows lower energy losses during charge–discharge cycles, indicating reduced internal resistances and improved charge transfer kinetics.

The BN/α-Fe_2O_3 with 73.2% efficiency experiences greater energy dissipation than the PEG-assisted composite. It is also evident that the PEG-BN/α-Fe_2O_3 composite retains about 85% of its capacitance after 5000 cycles, whereas BN/α-Fe_2O_3 retains only 75%, displaying better cycling stability in the PEG-assisted composite. This improved retention is attributed to PEG's role in maintaining electrode integrity and eliminating capacity loss over time.

The cyclic stability of PEG-BN/α-Fe_2O_3 and BN/α-Fe_2O_3 composites is evaluated by monitoring the capacity retention (%) over multiple charge–discharge cycles (5000 cycles) as shown in Fig. 8. The long-term electrochemical performance of electrode materials is crucial in determining their viability for energy storage applications. Both the composites exhibited an initial decrease in capacitance in the first few cycles due to electrolyte penetration and surface redox transitions.[63] The PEG-BN/α-Fe_2O_3 composites show a slower decline in capacity retention over time indicating improved cyclic stability than BN/α-Fe_2O_3 composites. At 4000 cycles, PEG-BN/α-Fe_2O_3 composites retain approximately 85% of their initial capacitance, whereas BN/α-Fe_2O_3 composites stabilize around 75%.

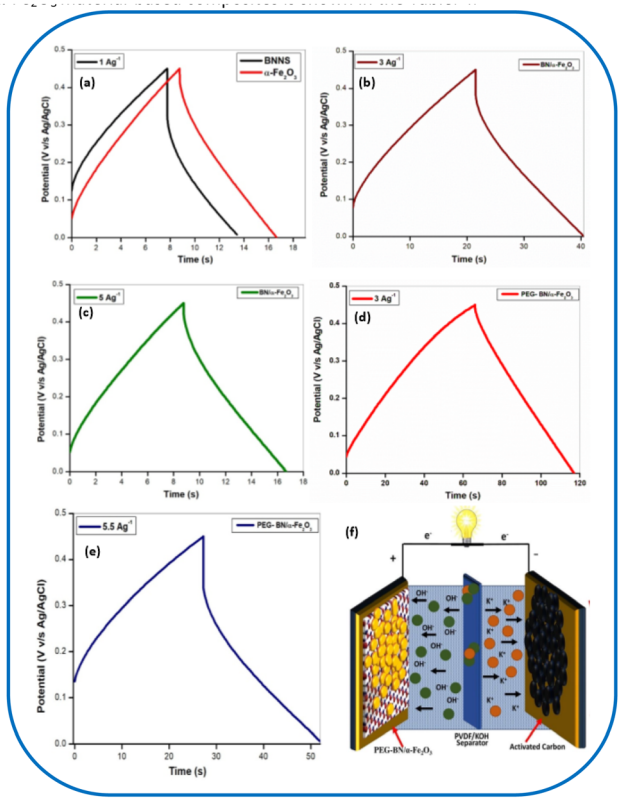

Fig. 7 Galvanostatic charge–discharge analysis at varying current densities (a) BN & α-Fe_2O_3 at 1 A g^{-1}, (b) BN/α-Fe_2O_3 at 3 A g^{-1}, (c) BN/α-Fe_2O_3 at 5 A g^{-1}, (d) PEG-BN/α-Fe_2O_3 at 3 A g^{-1}, and (e) PEG-BN/α-Fe_2O_3 composites that 5.5 A g^{-1}, (f) graphical representation of charge–discharge process of composites.

Table 4 The comparison of electrochemical performances of BN and α-Fe_2O_3 material-based hybrid composites

Composites	Synthesis routes	Electrolyte used	Voltage window (V)	Specific capacitance (F g^{-1})	Cyclic stability retention rate (cycles) with (ref.)
PEG-BN/α-Fe_2O_3 (as reported in this work)	Hydrothermal	6M KOH	0 to 0.5	361.6 F g^{-1} at 3 A g^{-1}	85% after 5000 cycles
h-BNNS/rGO	Hydrothermal	1M Na_2SO_4	−0.9 to 0.9	48.5 at 2 A g^{-1}	107% after 5000 cycles (ref. 55)
BN/rGO/Co_3O_4	Hydrothermal	1M KOH	0 to 3	145.7 at 6 A g^{-1}	78% after 5000 cycles (ref. 56)
BN/CNT/PANI	Chemical oxidative polymerization	1M H_2SO_4	0 to 2	387.5 at 1 A g^{-1}	87% after 6000 cycles (ref. 57)
BN/Graphene/MOS_2	Ball milling and ultrasonication	6M KOH	−0.4 to 0.5	423 at 1 A g^{-1}	96.4% after 10 000 cycles (ref. 58)
α-Fe_2O_3/rGO	Hydrothermal	1M KOH	−1.1 to 0.3	908 at 2 A g^{-1}	76% after 2000 cycles (ref. 59)
α-Fe_2O_3/Graphene	Ion adsorption	2M KOH	−1 to 0	264 at 2.5 A g^{-1}	85.7% after 1000 cycles (ref. 60)
CNT/α-Fe_2O_3	Hydrothermal	2M KCl	−1 to 0	296 at 5 mV s^{-1}	60% after 1000cycles (ref. 61)
α-Fe_2O_3/Graphene oxide/ Polypyrrole	Electrodeposition	1M KCl	−0.1 to 0.7	442.7 at 1 A g^{-1}	88% after 8000cycles (ref. 62)

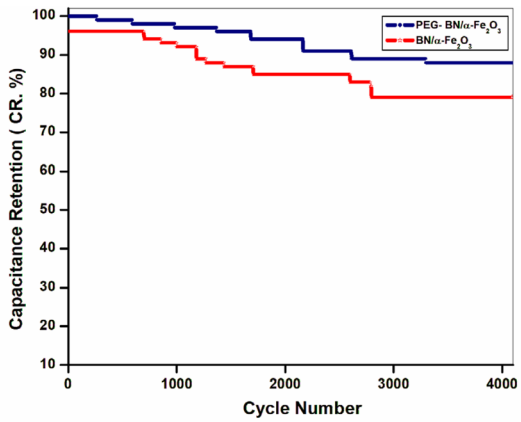

Fig. 8 Cyclic stability determination of hydrothermally prepared BN/α-Fe_2O_3 and PEG-BN/α-Fe_2O_3 composites obtained after 1st and 5000 cycles, capacitance retention (%) *versus* cycle number.

This enhanced stability is attributed to the improved dispersion and interfacial contact facilitated by PEG, which minimized the electrode degradation during repeated charge–discharge cycles. It is noted that during repeated charge–discharge cycles, volume expansion and contraction lead to structural stress within any composite material, further reducing the efficiency and capacitance.[64] PEG forms a flexible network within the composite, accommodating volume fluctuations, thus preventing structural breakdown. The rate capability of BN/α-Fe_2O_3 and PEG-BN/α-Fe_2O_3 composites is investigated by measuring the specific capacitance at different current densities ranging from 3 to 5 A g^{-1} as denoted in Fig. 9(a and b). Both the composites exhibited a decrease in specific capacitance with increasing current densities, a common characteristic observed in electrochemical capacitors due to kinetic limitations of ion diffusion at higher rates.[65]

However, the PEG-BN/α-Fe_2O_3 composite consistently demonstrated a higher specific capacitance value compared to the BN/α-Fe_2O_3 composite across all current densities. At a current density of 3 A g^{-1} PEG-BN/α-Fe_2O_3 delivered a specific capacitance of 361.6 F g^{-1}, while BN/α-Fe_2O_3 exhibited a capacitance of 125.8 F g^{-1}.

A two-probe method is employed for *I–V* measurements. Solid pellets with a thickness of 1 mm and a diameter of 4 mm were prepared using a hydraulic press. The *I–V* characteristics of BN/α-Fe_2O_3 and PEG-BN/α-Fe_2O_3 are depicted in Fig. 9(c) and (d) respectively. The *I–V* curve of α-Fe_2O_3 shows a nonlinear S-shaped behavior curve, indicating its semiconductor nature.[66] The *I–V* curve of BN appears flat, exhibiting insulating or highly resistive behavior due to its wide bandgap.[67] The PEG-BN/α-Fe_2O_3 composites show a higher current response under the same voltage window than BN/α-Fe_2O_3 indicating better electrical conductivity and improved charge carrier transport. BN

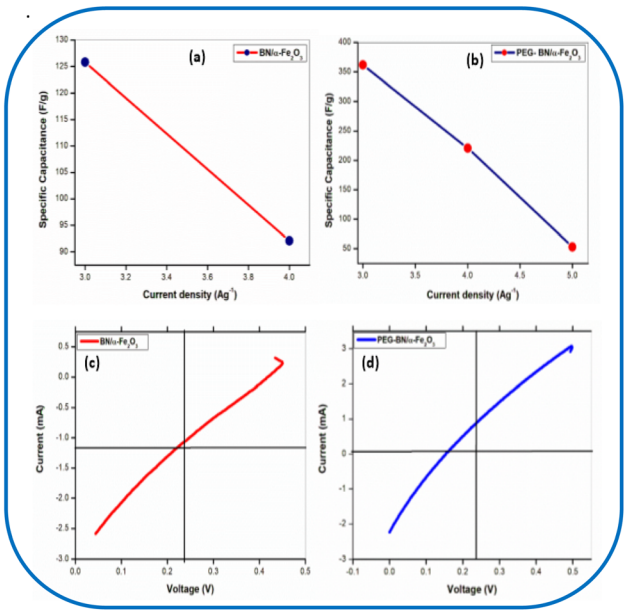

Fig. 9 Illustrates the variation of specific capacitance with an increase in current density for (a) BN/α-Fe_2O_3 and (b) PEG-BN/α-Fe_2O_3 composites produced by hydrothermal process, and the *I–V* measurements of hydrothermally synthesized (c) BN/α-Fe_2O_3 and (d) PEG-BN/α-Fe_2O_3 composites to analyze their electrical behavior.

with a large band gap acts as an insulator, but when combined with α-Fe_2O_3 influences the charge transport by further modifying the interface and facilitating electron flow. The presence of PEG enhances electron mobility by reducing charge trapping and improving interfacial connectivity, making it a better-conducting material.[68] Electrochemical impedance spectroscopy (EIS)measurements are performed to evaluate the charge transfer properties of BN/α-Fe_2O_3 and PEG-BN/α-Fe_2O_3 composites. The resulting Nyquist plots represent the relationship between the real Z_r and imaginary Z_i components of impedance for BN/α-Fe_2O_3 and PEG-BN/α-Fe_2O_3 composites are denoted in Fig. 10(a) and (b) respectively.

The BN/α-Fe_2O_3 composites exhibited a large distorted semicircle followed by a sloped line at higher frequencies, suggesting the presence of both resistive and capacitive components. The PEG-BN/α-Fe_2O_3 composites display a smaller semicircle and a more gradual slope, indicating reduced charge transfer resistance. The potential IR drop in electrochemical applications determines the voltage caused by the resistive components within the system, usually including the charge transfer, electrolyte, and contact resistance.[69] Equivalent circuits are developed to evaluate the potential of these composites for supercapacitor applications.[48] A potential drop of 82 mV and 39.70 mV, respectively, at a current density of 3 A g^{-1} is observed on BN/α-Fe_2O_3 and PEG-BN/α-Fe_2O_3 composites. The substantial reduction of IR drop in PEG-BN/α-Fe_2O_3 composite indicates a minimal energy dissipation during fast charge–discharge cycles, improving the efficiency under practical working conditions. This also corresponds to minimal heating during operation, thus contributing to the long-term stability as well as the durability of the electrode system,

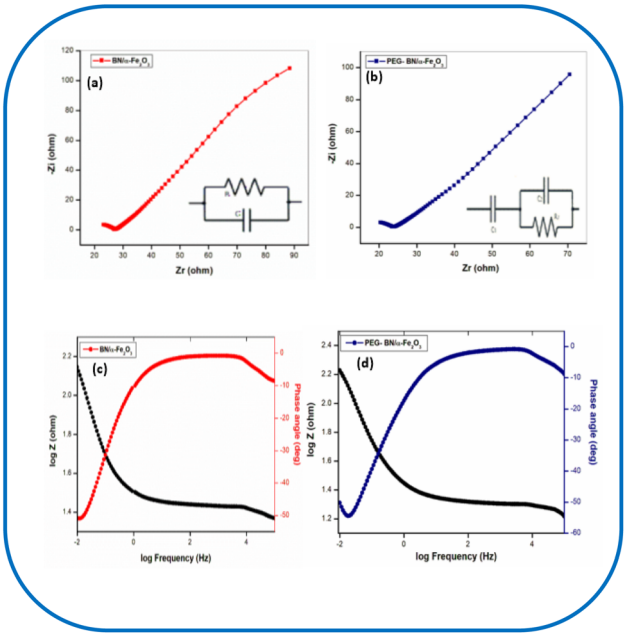

Fig. 10 Nyquist plots for (a) BN/α-Fe_2O_3 and (b) PEG-BN/α-Fe_2O_3 composites and bode plots for (c) BN/α-Fe_2O_3 and (d) PEG-BN/α-Fe_2O_3 composites synthesized *via* the hydrothermal method.

addressing the key challenge faced in supercapacitor applications. In BN/α-Fe_2O_3 composites, the equivalent circuit consists of charge transfer resistance (R_{CT}) ($R_{CT} = 27.378$ mΩ) in parallel with a single capacitor ($C = 103.38$ F). This configuration indicates a fundamental charge storage mechanism with moderate capacitance. The equivalent circuit of PEG-BN/α-Fe_2O_3 composites includes two capacitors, C1 = 149.09 mF and C2 = 103.75 F, along with a charge transfer resistance($R_{CT} = 13.234$ mΩ) and storage capability, further enhancing the supercapacitor performance. The additional series capacitance C1 in PEG-BN/α-Fe_2O_3 composites contributes to higher charge storage efficiency and lower internal resistance, compared to BN/α-Fe_2O_3 composites, factors crucial for long-term stability. The Bode plot represents the relation between impedance (log Z) and frequency, depicting the phase angle variation as demonstrated in Fig. 10(c) and (d) consecutively. The log Z value decreases with increasing frequency, for both composites indicating a transition from resistive to capacitive behavior. The log Z value of PEG-BN/α-Fe_2O_3 composites is higher at lower frequencies, but it decreases more rapidly, indicating enhanced conductivity. At lower frequencies, the impedance of both composites remains high, indicating limited charge transfer mobility and a significant contribution from charge transfer resistance (R_{CT}).

However, PEG-BN/α-Fe_2O_3 composites exhibit a relatively higher impedance in this region, depicting a more effective charge accumulation mechanism due to improved interfacial interactions and electrolyte accessibility. The sharp decrease in impedance at higher frequencies is attributed to the ability of PEG to improve electrode wettability, ion diffusion, and efficient charge transport mechanisms. A higher phase angle shift also suggests that PEG-BN/α-Fe_2O_3 composites elucidate efficient capacitive behavior making it a superior choice for supercapacitor applications.[70] These experimental results highlight that the strategic integration of BN and α-Fe_2O_3 assisted by PEG modification serves as an excellent approach for tailoring material properties and broadening the applicability of these materials in energy storage and conversion technologies.

4. Conclusion

A novel hybrid nanocomposite composed of boron nitride (BN), and hematite(α-Fe_2O_3), assisted by PEG modification, has been successfully synthesized using a combination of ultrasonication and hydrothermal treatment methods. This hybrid takes advantage of affordable materials-polyethylene glycol (PEG), boron nitride (BN), and hematite (α-Fe_2O_3)—and efficient synthesis to generate an economically affordable material system that is not compromised in its performance.[71–76] The TGA analysis confirms the exceptional stability of the prepared nanocomposites. Notably, PEG-BN/α-Fe_2O_3 composites demonstrate the highest thermal stability among all composites, as PEG acts as a thermal buffer, enhancing interfacial buffer bonding and delaying decomposition at elevated temperatures. The crystallite size and corresponding lattice strain are calculated from the XRD analysis, validating the

successful formation of the nanocomposite and providing clear evidence of its phase composition. FTIR studies substantiate the presence of Fe–O and B–N bonds in the composites, along with O–H stretching vibrations from PEG, indicating successful composite formation and strong molecular interaction. Raman spectroscopy further verified the presence of BN and α-Fe_2O_3, revealing a shift in Fe–O stretching vibrations in the composites, suggesting Fe–O–B interactions. The presence of PEG is confirmed by the observation of C–H bending vibrations. UV-visible spectroscopy affirms a reduction in the bandgap of both BN/α-Fe_2O_3(3.28 eV) and PEG-BN/α-Fe_2O_3(3.06 eV) compared to BN(5.9 eV), with a further decrease observed upon the addition of PEG. This reduction is attributed to improved charge transfer and electronic interactions facilitated by PEG, which acts as a surfactant and modifies the electric environment. Tauc plot analysis corroborated the bandgap values obtained from UV-visible analysis. The CV and GCD studies revealed that PEG-BN/α-Fe_2O_3 composites exhibit a higher specific capacitance value (361.6 F g^{-1} at 3 A g^{-1}) compared to BN/α-Fe_2O_3 (125.8 F g^{-1} at 3 A g^{-1}) and the individual components. BN provides increased surface area and improved mobility, while PEG enhances the electrode–electrolyte interaction, leading to better stability and cyclic performance. This is evident in the long-term cyclic stability tests, where PEG-BN/α-Fe_2O_3 composites retained 85% of their capacitance after 5000 cycles, compared to 75% for BN/α-Fe_2O_3 composites. The electrochemical analysis indicates that PEG-assisted composite significantly shows an enhancement in their charge storage capability and conductivity, making them more suitable for supercapacitor applications. The reduction in charge transfer mechanism, the presence of additional capacitance elements, and the improved phase angle shift collectively demonstrate the superior capacitive behavior of PEG-BN/α-Fe_2O_3 composites. This work presents a promising new pathway for developing cost-effective, highly active materials with diverse functionalities. Furthermore, the successful synthesis and characterization of innovative hybrid composites (BN/α-Fe_2O_3 & PEG-BN/α-Fe_2O_3 composites) pave the way for advancements in material science, potentially leading to more efficient and affordable energy technologies.

Data availability

The data that support the findings of this study are available from the corresponding author upon reasonable request.

Conflicts of interest

There are no conflicts to declare.

Acknowledgements

The authors express their sincere gratitude to Noorul Islam Centre for Higher Education, Tamil Nadu, and the Department of Science and Technology (DST), New Delhi, for their support and for providing the fellowship (IF 190811), which facilitated the completion of this research work. This project was supported by the Researchers Supporting Project number (RSP2025R238), King Saud University, Riyadh, Saudi Arabia. This project was also supported by the National Research Foundation of Korea (NRF) (Grant no: 2020R1A6A1A03044512).

References

1 J. Mitali, S. Dhinakaran and A. A. Mohamad, Energy storage systems: a review, *Energy Storage Sav.*, 2022, **1**(3), 166–216.
2 S. Sagadevan, A. R. Marlinda, Z. Z. Chowdhury, Y. B. A. Wahab, N. A. Hamizi and M. M. Shahid, *et al.*, Fundamental electrochemical energy storage systems, in *Advances in Supercapacitor and Supercapattery*, Elsevier eBooks, 2020, pp. 27–43.
3 S. Shams and B. Bindhu, Recent advancements in hybrid two dimensional materials for energy applications, *ES Energy Environ.*, 2024, **24**, 1160.
4 T. Liu, J. Ding, Z. Su and G. Wei, Porous two-dimensional materials for energy applications: Innovations and challenges, *Mater. Today Energy*, 2017, **6**, 79–95.
5 S. Roy, X. Zhang, A. B. Puthirath, A. Meiyazhagan, S. Bhattacharyya, M. M. Rahman, G. Babu, S. Susarla, S. K. Saju, M. K. Tran and L. M. Sassi, Structure, properties and applications of two-dimensional hexagonal boron nitride, *Adv. Mater.*, 2021, **33**(44), 2101589.
6 C. Chen, Y. Xie, M. Zhang, J. Li, X. Wei and Z. Zhang, Significantly enhanced energy storage properties in sandwich-structured polymer composites with self-assembled boron nitride layers, *Appl. Surf. Sci.*, 2022, **598**, 153673.
7 T. Divya, R. Sarankumar, K. S. Balamurugan, P. Sakthivel and A. Sivakami, Recent advances in transition metal oxide composites for enhanced supercapacitor performance: a comprehensive overview, *J. Nanopart. Res.*, 2025, **27**(2), 55.
8 S. N. Hussein, B. M. Jan, M. Khalil, Z. Amir and A. Azizi, Surface modification of superparamagnetic nanoparticles for enhanced oil recovery: A review, *J. Mol. Liq.*, 2024, **397**, 124146.
9 T. Qin, X. Zhao, Y. Sui, D. Wang, W. Chen, Y. Zhang, S. Luo, W. Pan, Z. Guo and D. Y. Leung, Heterointerfaces: unlocking superior capacity and rapid mass transfer dynamics in energy storage electrodes, *Adv. Mater.*, 2024, **36**(32), 2402644.
10 Y. Li, M. S. Yao, Y. He and S. Du, Recent Advances of Electrocatalysts and Electrodes for Direct Formic Acid Fuel Cells: from Nano to Meter Scale Challenges, *Nano–Micro Lett.*, 2025, **17**(1), 148.
11 X. Zheng, Z. Song, D. Zhang, W. Du, L. Miao, Y. Lv, L. Xie, L. Gan and M. Liu, Rational design of a dual-gradient zincophilic–conductive interphase for dendrite-free zinc batteries, *J. Mater. Chem. A*, 2024, **12**(25), 15352–15360.
12 Y. Shu, T. Zhao, Y. Li, L. Yang, X. Li, G. Feng, W. Jia and F. Luo, Porous Fe/FeO/Fe_2O_3 nanorod/RGO composites with high-efficiency electromagnetic wave absorption property, *Appl. Surf. Sci.*, 2023, **626**, 157223.
13 W. Yang, Z. Gao, J. Wang, B. Wang and L. Liu, Hydrothermal synthesis of reduced graphene sheets/Fe_2O_3 nanorods composites and their enhanced electrochemical

performance for supercapacitors, *Solid State Sci.*, 2013, **20**, 46–53.

14 W. C. Lai, C. W. Chang and C. Y. Hsueh, Shape-stabilized poly (ethylene glycol) phase change materials with self-assembled network scaffolds for thermal energy storage, *Polymer*, 2021, **213**, 123196.

15 A. Kim, N. A. Wert, E. B. Gowd and R. Patel, Recent progress in PEG-based composite phase change materials, *Polym. Rev.*, 2023, **63**(4), 1078–1129.

16 A. Sarcinella, J. L. de Aguiar, C. Jesus and M. Frigione, Thermal properties of PEG-based form-stable Phase Change Materials (PCMs) incorporated in mortars for energy efficiency of buildings, *J. Energy Storage*, 2023, **67**, 107545.

17 E. Karthikraja, C. Chowdhury, N. V. Nulakani, K. Ramanujam, V. G. Vaidyanathan and V. Subramanian, Transition Metal Anchored Novel Holey Boron Nitride Analogues as Single-Atom Catalysts for the Hydrogen Evolution Reaction, *Chem.–Asian J.*, 2025, **20**(3), e202401256.

18 J. Y. Chung, B. Lee, I. K. Park, H. H. Park, H. S. Jung, J. C. Park, H. C. Cho and J. D. Nam, High thermal conductive natural rubber composites using aluminum nitride and boron nitride hybrid fillers, *Elastomers Compos.*, 2020, **55**(1), 59–66.

19 R. Hu, S. Wen, Q. Chen, X. Sun, H. Liu, W. Gao and Y. Bai, Universal Construction of Electrical Insulation and High-Thermal-Conductivity Composites Based on the *In Situ* Exfoliation of Boron Nitride-Graphene Hybrid Filler, *ACS Appl. Mater. Interfaces*, 2025, **17**(4), 6783–6792.

20 D. Hassan, M. K. Mohammed and A. Hashim, Fabrication and improved optical properties of PEG/Fe_2O_3 nanocomposites, *World J. Adv. Res. Rev.*, 2023, **17**(1), 1186–1193.

21 R. Anjana, D. P. Hanamantrao, G. N. Banu, V. Raja, R. R. Isaac, J. S. John, K. Vediappan, S. P. Jose, B. Neppolian and D. Sajan, Hydrothermal synthesis of graphitic carbon nitride/Ce doped Fe2O3 heterostructures for supercapattery device and hydrogen evolution reaction, *J. Energy Storage*, 2025, **116**, 116021.

22 R. B. Chrisma, R. I. Jafri and E. I. Anila, A review on the electrochemical behavior of graphene–transition metal oxide nanocomposites for energy storage applications, *J. Mater. Sci.*, 2023, **58**(14), 6124–6150.

23 X. Yang, C. Hu, Y. Chen, Z. Song, L. Miao, Y. Lv, H. Duan, M. Liu and L. Gan, Tailoring ion-accessible pores of robust nitrogen heteroatomic carbon nanoparticles for high-capacity and long-life Zn-ion storage, *J. Energy Storage*, 2024, **104**, 114509.

24 M. A. Al, A. H. Alshatteri, H. S. Alhasan, W. Al Zoubi, K. M. Omer and M. R. Thalji, Copper-doped strontium metal-organic framework: Dual-function active material for supercapacitor and oxygen evolution reaction, *Electrochim. Acta*, 2024, **503**, 144857.

25 S. Shams, B. Bindhu, A. Murali, R. Ramesh, A. Al Souwaileh and S. S. Han, High-performance boron nitride/graphene oxide composites modified with sodium thiosulfate for energy storage applications, *Nanoscale Adv.*, 2025, **7**, 1803–1813.

26 P. Thangasamy and M. Sathish, Dwindling the re-stacking by simultaneous exfoliation of boron nitride and decoration of α-Fe 2 O 3 nanoparticles using a solvothermal route, *New J. Chem.*, 2018, **42**(7), 5090–5095.

27 D. Liu, Y. Wang, Q. Gong, Y. Xia, L. Li, Y. Xue, J. Yang and S. Li, Modification Strategies of Hexagonal Boron Nitride Nanomaterials for Photocatalysis, *Chem. Rec.*, 2024, **24**(7), e202300334.

28 H. Wang, J. Mao, Z. Zhang, Q. Zhang, L. Zhang, W. Zhang and P. Li, Photocatalytic degradation of deoxynivalenol over dendritic-like α-Fe2O3 under visible light irradiation, *Toxins*, 2019, **11**(2), 105.

29 H. Jeong, J. Kim, D. Y. Kim, J. Kim, S. Moon, O. F. Ngome Okello, S. Lee, H. Hwang, S. Y. Choi and J. K. Kim, Resistive switching in few-layer hexagonal boron nitride mediated by defects and interfacial charge transfer, *ACS Appl. Mater. Interfaces*, 2020, **12**(41), 46288–46295.

30 M. Mohammadi, F. Alirezapour and A. Khanmohammadi, Adsorption of transition metal cations (Cr^{2+}, Mn^{2+}, Fe^{2+}, Cu+, Ag+ and Au+) on boron nitride nanotube: structural analysis and electronic properties, *Adv. J. Chem., Sect. A*, 2024, **7**(4), 355–373.

31 Y. Xu, Z. Huang, Z. Zhang, B. Ding, P. Li, J. Liu, Y. Hao, L. Dai, H. Zhang, C. Zhu and W. Cai, An electro-optical Kerr device based on 2D boron nitride liquid crystals for solar-blind communications, *Adv. Mater.*, 2024, **36**(26), 2307330.

32 A. Azme, I. C. Escobar, O. Tsyusko and N. Aich, Effects of two wet exfoliation strategies on the yield and colloidal behavior of 2D hexagonal boron nitride nanosheets, *Nano Express*, 2025, **6**, 015011.

33 K. Inoue, T. Goto, M. Iida, T. Ito, Y. Shimizu, Y. Hakuta and K. Terashima, Aqueous dispersion of hexagonal boron nitride *via* plasma processing in a hydroquinone solution, *J. Phys. D: Appl. Phys.*, 2020, **53**(42), 42LT01.

34 X. Hou, Z. Yu, Y. Li and K. C. Chou, Preparation and properties of hexagonal boron nitride fibers used as high temperature membrane filter, *Mater. Res. Bull.*, 2014, **49**, 39–43.

35 A. K. Tripathi, M. C. Mathpal, P. Kumar, V. Agrahari, M. K. Singh, S. K. Mishra, M. M. Ahmad and A. Agarwal, Photoluminescence and photoconductivity of Ni doped titania nanoparticles, *Adv. Mater. Lett.*, 2015, **6**(3), 201–208.

36 Y. Chen, Z. Shi, S. Zhang, J. Ben, K. Jiang, H. Zang, Y. Jia, W. Lü, D. Li and X. Sun, The van der Waals Epitaxy of High-Quality N-Polar Gallium Nitride for High-Response Ultraviolet Photodetectors with Polarization Electric Field Modulation, *Adv. Electron. Mater.*, 2022, **8**(1), 2100759.

37 E. Darezereshki, F. Bakhtiari, M. Alizadeh and M. Ranjbar, Direct thermal decomposition synthesis and characterization of hematite (α-Fe_2O_3) nanoparticles, *Mater. Sci. Semicond. Process.*, 2012, **15**(1), 91–97.

38 E. Darezereshki, One-step synthesis of hematite (α-Fe_2O_3) nano-particles by direct thermal-decomposition of maghemite, *Mater. Lett.*, 2011, **65**(4), 642–645.

39 N. S. Vrandečić, M. Erceg, M. Jakić and I. Klarić, Kinetic analysis of thermal degradation of poly (ethylene glycol) and poly (ethylene oxide) s of different molecular weight, *Thermochim. Acta*, 2010, **498**(1), 71–80.

40 C. Lohaus, C. Steinert, J. Brötz, A. Klein and W. Jaegermann, Systematic investigation of the electronic structure of hematite thin films, *Adv. Mater. Interfaces*, 2017, **4**(20), 1700542.

41 R. Y. Tay, M. H. Griep, G. Mallick, S. H. Tsang, R. S. Singh, T. Tumlin, E. H. Teo and S. P. Karna, Growth of large single-crystalline two-dimensional boron nitride hexagons on electropolished copper, *Nano Lett.*, 2014, **14**(2), 839–846.

42 N. Ajinkya, X. Yu, P. Kaithal, H. Luo, P. Somani and S. Ramakrishna, Magnetic iron oxide nanoparticle (IONP) synthesis to applications: present and future, *Materials*, 2020, **13**(20), 4644.

43 K. Watanabe, T. Taniguchi and H. Kanda, Direct-bandgap properties and evidence for ultraviolet lasing of hexagonal boron nitride single crystal, *Nat. Mater.*, 2004, **3**(6), 404–409.

44 M. Seki and H. Tabata. Functional Iron Oxides and Their Heterostructures, *Correlated Functional Oxides: Nanocomposites and Heterostructures*, 2017, pp. 1–28.

45 H. Liu, Y. Chen, M. Yang and J. Gu, Strategies for enhancing capacity and rate performance of two-dimensional material-based supercapacitors, *Acta Phys.-Chim. Sin.*, 2025, **41**(6), 100063.

46 M. Müllner and A. H. Müller, Cylindrical polymer brushes–Anisotropic building blocks, unimolecular templates and particulate nanocarriers, *Polymer*, 2016, **98**, 389–401.

47 D. Sheng, X. Liu, Z. Yang, M. Zhang, Y. Li, P. Ren, X. Yan, Z. X. Shen and D. Chao, Hydrogen Bond Network Regulation in Electrolyte Structure for Zn-based Aqueous Batteries, *Adv. Funct. Mater.*, 2024, **34**(37), 2402014.

48 Z. Liu, B. Sun, Y. Zhang, Q. Zhang and L. Fan, Polymer-adjusted zinc anode towards high-performance aqueous zinc ion batteries, *Prog. Polym. Sci.*, 2024, 101817.

49 V. D. Nithya and N. S. Arul, Review on α-Fe_2O_3 based negative electrode for high performance supercapacitors, *J. Power Sources*, 2016, **327**, 297–318.

50 V. Guerra, C. Wan and T. McNally, Thermal conductivity of 2D nano-structured boron nitride (BN) and its composites with polymers, *Prog. Mater. Sci.*, 2019, **100**, 170–186.

51 D. Govindarajan, M. Selvaraj, W. Limphirat, K. Kirubaharan, G. Murugadoos, J. Theerthagiri, M. Y. Choi and S. Kheawhom, Synergistic effects of haematite/hausmannite anchored graphene hybrids in high-energy density asymmetric supercapacitors, *J. Alloys Compd.*, 2024, **1004**, 175949.

52 H. Liu, Y. Chen, M. Yang and J. Gu, Strategies for enhancing capacity and rate performance of two-dimensional material-based supercapacitors, *Acta Phys.–Chim. Sin.*, 2025, **41**(6), 100063.

53 G. Li, X. Gao, K. Wang and Z. Cheng, Porous carbon nanospheres with high EDLC capacitance, *Diamond Relat. Mater.*, 2018, **88**, 12–17.

54 T. S. Mathis, N. Kurra, X. Wang, D. Pinto, P. Simon and Y. Gogotsi, Energy storage data reporting in perspective—guidelines for interpreting the performance of electrochemical energy storage systems, *Adv. Energy Mater.*, 2019, **9**(39), 1902007.

55 T. Yang, H. J. Liu, F. Bai, E. H. Wang, J. H. Chen, K. C. Chou and X. M. Hou, Supercapacitor electrode based on few-layer h-BNNSs/rGO composite for wide-temperature-range operation with robust stable cycling performance, *Int. J. Miner. Metall. Mater.*, 2020, **27**, 220–231.

56 N. Althubaiti, Y. Mussa, C. S. Bongu, Z. Bayhan, M. Arsalan, A. Soliman and E. Alsharaeh, Reduced graphene oxide/hexagonal boron nitride-based composite as a positive electrode in asymmetric supercapacitors, *J. Mater. Sci.*, 2022, **57**(30), 14371–14385.

57 C. K. Maity, G. Hatui, S. Sahoo, P. Saren and G. C. Nayak, Boron nitride based ternary nanocomposites with different carbonaceous materials decorated by polyaniline for supercapacitor application, *ChemistrySelect*, 2019, **4**(13), 3672–3680.

58 C. S. Bongu, M. Arsalan and E. H. Alsharaeh, 2D hybrid nanocomposite materials (h-BN/G/MoS2) as a high-performance supercapacitor electrode, *ACS Omega*, 2024, **9**(13), 15294–15303.

59 H. Wang, Z. Xu, H. Yi, H. Wei, Z. Guo and X. Wang, One-step preparation of single-crystalline Fe2O3 particles/graphene composite hydrogels as high performance anode materials for supercapacitors, *Nano Energy*, 2014, **7**, 86–96.

60 J. Wu, A. Zhou, Z. Huang, L. Li and H. Bai, A Facile Method to Prepare Three-Dimensional Fe_2O_3/Graphene Composites as the Electrode Materials for Supercapacitors, *Chin. J. Chem.*, 2016, **34**(1), 67–72.

61 X. Cheng, X. Gui, Z. Lin, Y. Zheng, M. Liu, R. Zhan, Y. Zhu and Z. Tang, Three-dimensional α-Fe 2 O 3/carbon nanotube sponges as flexible supercapacitor electrodes, *J. Mater. Chem. A*, 2015, **3**(42), 20927–20934.

62 J. Vigneshwaran, S. Abraham, B. Muniyandi, T. Prasankumar, J. T. Li and S. Jose, Fe_2O_3 decorated graphene oxide/polypyrrole matrix for high energy density flexible supercapacitor, *Surf. Interfaces*, 2021, **27**, 101572.

63 W. Pholauyphon, P. Charoen-amornkitt, T. Suzuki and S. Tsushima, Guidelines for supercapacitor electrochemical analysis: A comprehensive review of methodologies for finding charge storage mechanisms, *J. Energy Storage*, 2024, **98**, 112833.

64 J. P. Thomas, W. R. Pogue III, G. T. Pham and S. M. Qidwai, Flexure and pressure-loading effects on the performance of structure–battery composite beams, *J. Compos. Mater.*, 2019, **53**(20), 2863–2874.

65 N. P. Ngidi, A. F. Koekemoer and S. S. Ndlela, Application of metal oxide/porous carbon nanocomposites in electrochemical capacitors: A mini-review, *Phys. Chem. Earth, Parts A/B/C*, 2024, 103698.

66 M. Y. Perdana, B. A. Johan, M. Abdallah, M. E. Hossain, M. A. Aziz, T. N. Baroud and Q. A. Drmosh, Understanding the behavior of supercapacitor materials *via* electrochemical impedance spectroscopy: a review, *Chem. Rec.*, 2024, **24**(5), e202400007.

67 K. J. Noh, H. J. Oh, B. R. Kim, S. C. Jung, W. Kang and S. J. Kim, Photoelectrochemical Properties of Fe2O3 Supported on TiO2-Based Thin Films Converted from Self-Assembled Hydrogen Titanate Nanotube Powders, *J. Nanomater.*, 2012, **2012**(1), 475430.

68 W. Lin, P. Zhuang, D. Akinwande, X. A. Zhang and W. Cai, Oxygen-assisted synthesis of hBN films for resistive random access memories, *Appl. Phys. Lett.*, 2019, **115**, 073101.

69 M. Marcinek, J. Syzdek, M. Marczewski, M. Piszcz, L. Niedzicki, M. Kalita, A. Plewa-Marczewska, A. Bitner, P. Wieczorek, T. Trzeciak and M. Kasprzyk, Electrolytes for Li-ion transport–Review, *Solid State Ionics*, 2015, **276**, 107–126.

70 C. Lu and X. Chen, Latest advances in flexible symmetric supercapacitors: from material engineering to wearable applications, *Acc. Chem. Res.*, 2020, **53**(8), 1468–1477.

71 P. G. Ghuge, C. V. More, M. I. Sayyed, Y. Maghrbi and P. P. Pawar, Smart polymers as gamma ray Shields: Experimental evaluation of shielding performance, *J. Radiat. Res. Appl. Sci.*, 2025, **18**(2), 101398.

72 S. Mishra and B. K. Jena, Review and Perspectives on Multifunctional Applications of Hexagonal Boron Nitride Nanosheets and Quantum Dots in Energy Conversions, *Energy Fuels*, 2025, **39**(9), 4119–4150.

73 K. C. Verma, N. Goyal, M. Singh, M. Singh and R. K. Kotnala, Hematite α-Fe_2O_3 induced magnetic and electrical behavior of $NiFe_2O_4$ and $CoFe_2O_4$ ferrite nanoparticles, *Results Phys.*, 2019, **13**, 102212.

74 L. Upadhyay, S. Dhanapandian, S. Suthakaran, B. Yadav, K. K. Kar, D. Kumar and J. Arikrishnan, Investigation of physicochemical and electrochemical traits of hydrothermally synthesized α-Fe_2O_3 nanoparticles for supercapacitor performance, *J. Mater. Sci.: Mater. Electron.*, 2025, **36**(2), 136.

75 K. W. Juvencio, L. A. Contreras Alvarez, A. M. Gomes, F. Vasconcelos Campos, J. P. Oliveira and M. C. Guimarães, Optimized Synthesis and Stabilization of Superparamagnetic Iron Oxide Nanoparticles for Enhanced Biomolecule Adsorption, *ACS Omega*, 2025, **10**(2), 1976–1987.

76 M. Li, S. Han, C. Dan, T. Wu, F. You, X. Jiang, Y. Wu and Z. M. Dang, Boron Nitride-Polymer Composites with High Thermal Conductivity: Preparation, Functionalization Strategy and Innovative Structural Regulation, *Small*, 2025, 2412447.